

Potential of Nb₂O₅ nanofibers in photocatalytic response for organic pollutants remediation

Edson Tobias Jesus

IFMA: Instituto Federal de Educacao Ciencia e Tecnologia do Maranhao

Ailton José Moreira

UFSCar CCET: Universidade Federal de Sao Carlos Centro de Ciencias Exatas e de Tecnologia

Mayara Coelho Sá

IFMA: Instituto Federal de Educacao Ciencia e Tecnologia do Maranhao

Gian Paulo Giovanni Freschi

UNIFAL-MG: Universidade Federal de Alfenas

Miryam Rincón Joya

Universidad Nacional de Colombia

Maximo Siu Li

Universidade de São Paulo Instituto de Física de São Carlos: Universidade de Sao Paulo Instituto de Fisica de Sao Carlos

Elaine Cristina Paris (✉ elaine.paris@embrapa.br)

Embrapa Instrumentação <https://orcid.org/0000-0001-8599-9674>

Research Article

Keywords: Photocatalysis, Organic pollutant, Drug, Ceramic nanofiber, Electrospinning

Posted Date: April 19th, 2021

DOI: <https://doi.org/10.21203/rs.3.rs-334663/v1>

License:  This work is licensed under a Creative Commons Attribution 4.0 International License.

[Read Full License](#)

Version of Record: A version of this preprint was published at Environmental Science and Pollution Research on July 23rd, 2021. See the published version at <https://doi.org/10.1007/s11356-021-15435-8>.

Abstract

Due to the pollution caused by different organic pollutants, various photocatalytic nanomaterials for environmental remediation have been promoted. In this study, Nb_2O_5 nanofibers were obtained by electrospinning technique, presenting controlled crystallinity and high specific surface area to improve the photoactivity response. The structural characterization indicated Nb_2O_5 nanofibres with orthorhombic phase formation, and the photoluminescence measurements showed different energy levels contributing to the electronic transition events. The nanofibers with a bandgap up to 3.6 eV were applied to photocatalysis of dyes [Rhodamine B (RhB) or Methylene Blue (MB)], and Prozac®, listed as an emergent pollutant. In the optimized condition ($\text{pH} = 9$), the RhB and MB photocatalysis was 59% and 93% more efficient than photolysis due to $\zeta = -50 \pm 5 \text{ mV}$ for EtOH_550 sample that increased the interaction with MB (cationic) compared to RhB unprotonated ($\text{pKa} = 3.7$). Therefore, Prozac® ($\text{pKa} = 10.7$) was selected due to protonated form at $\text{pH} = 9$ and showed $68\% \pm 1$ adsorption in 30 min for EtOH_550. The Prozac® photocatalytic degradation under UV light irradiation was up to 17% higher than the photolytic degradation. The formation of hydroxyl radicals in the photocatalytic system (EtOH_550) was proven by the Coumarine probe assay, corroborating with the greater amount of α -[2-(Methylamino)ethyl]benzylalcohol (MAEB), a by-product obtained after Prozac® oxidation. Additionally, the material achieved specific catalytic activity for the different organic compounds (RhB, MB, or Prozac®), showing that only using dyes may not be ideal to conclude the great material applicability in environmental remediation studies. Therefore, Nb_2O_5 nanofibers were efficient for the degradation of three different pollutants under UV light, proving to be a viable alternative for environmental remediation.

Introduction

Pollution resulting from the inappropriate disposal of the varied industrial waste types has been the main route for contamination of environmental ecosystems (Kostich et al. 2014; Pinheiro et al. 2016; Lee et al. 2017). With the advancement of fine chemistry, new molecules have been created to meet society's demands in the fields of food (Kuenemann et al. 2017), health (Farooqui et al. 2018), agriculture (Sanaullah et al. 2020), and social well-being. Consequently, these new molecules have been increasingly introduced into ecosystems as contaminants, affecting environmental quality and increasing human health risks (Gouvêa et al. 2018; Grenni et al. 2018). Among these new molecules with high polluting potential, stand out the class of dyes, pesticides, and pharmaceutical products (Lapworth et al. 2012; Malafatti et al. 2020). Considering that environmental legislation does not keep up the speed with which these new molecules are created, this type of pollutant regulation is limited or non-existent in many countries (Petrie et al. 2015; Gorito et al. 2017). Watchful of this new reality, the scientific community has found in nanotechnology the appropriate tools to minimize the impacts of this type of pollution (Khan and Tahir 2019; Paris et al. 2020). In this sense, advanced oxidation technologies, especially heterogeneous photocatalysis, have been the most efficient tools to remove these emerging contaminants from environmental ecosystems (Védrine 2019).

The photocatalytic mechanism responsible for the degradation of organic pollutants is widely known. It can be summarized in the ability that materials with semiconductor properties exhibit to generate oxidizing (h^+) and reducing (e^-) sites on their surface (Rauf and Ashraf 2009; Gurgel et al. 2011). Therefore, when absorbing a photon, these materials promote the electron from the valence band (VB) to the conduction band (CB), giving rise to the electron/hole pair responsible for triggering the redox reactions (Oliveira et al. 2013; Shen et al. 2019). According to the literature, photocatalytic success is associated with the electronic photoexcitation efficiency, recombination processes decrease, active surface increase, the interaction between molecule/catalyst, and homogeneity of the catalyst in the reaction system (Fang et al. 2017; Moreira et al. 2020a). This property is also broadly correlated with the ceramic material crystalline structures (Paris et al. 2010), which can be influenced by the synthesis method (Leite et al. 2000) and heat treatment temperature (Alves et al. 2009). Therefore, TiO_2 application as a photocatalyst has been extensively investigated for environmental remediation, and nowadays, its physical-chemical modification has been proposed to optimize these processes (Shen et al. 2019). However, the search for alternative materials to TiO_2 has promoted significant advances in the field of heterogeneous photocatalysis, where semiconductors based on niobium oxide have been gaining prominence (Nico et al. 2016).

Nb_2O_5 as a photocatalyst for environmental remediation is still little reported compared to other semiconductors such as TiO_2 and ZnO . However, its photoactivity has shown to be promising (Raba et al. 2015; Falk et al. 2017). The structural properties of Nb_2O_5 favor chemical oxidation due to its ability to diffuse surface oxygen to form the reactive species $\cdot\text{O}_2^-$ and $\cdot\text{OH}$ (Nico et al. 2016). Moreover, the Nb_2O_5 surface characteristics highlight its adsorptive properties, favoring chemical conversions (Zhuang et al. 2016). By comparing the TiO_2 and Nb_2O_5 photoactivity, the niobium oxide structure electronic transitions are more varied, selecting its application in photocatalytic processes (Nb et al. 2018).

Thus, different synthesis methods have been investigated to obtain Nb_2O_5 (Nogueira et al. 2017; Falk et al. 2017; Silva et al. 2019). The precipitation method by dissolution in an aluminum reduction system supplied Nb_2O_5 in rod forms, and the photocatalytic properties for $\text{H}_{2(g)}$ production was evidenced (Zhao et al. 2016). Additionally, the evaporation-induced self-assembly (EISA) (Hashemzadeh et al. 2014), oxidant peroxide (Lopes et al. 2014), microwave-assisted (Falk et al. 2017), and polymeric precursors (Raba et al. 2015) methods were also applied to obtain Nb_2O_5 as a photocatalyst. When used for photocatalytic degradation of different organic pollutants, the efficiency is in the order of 45% for atrazine in 30 min (Lopes et al. 2014), > 95% for MB in 50 min (Shao et al. 2014), and > 45% for MB in 120 min (Falk et al. 2017). As an unconventional synthesis method, the electrospinning technique was applied to synthesize Nb_2O_5 nanofibers, exhibiting good performance to produce nanomaterials with structural defects that favor electromigration (Grishin et al. 2013). This method also had Nb_2O_5 with small particle diameters (21 to 37 nm) and high specific surface area (Leindecker et al. 2014). The Nb_2O_5 nanofiber photoactivity response was evaluated to the methyl orange degradation, reaching 62% in 3 h (Qi et al. 2013).

Under specific heat treatment conditions, the textural properties of Nb₂O₅ fibers can be controlled to become optimal adsorbents for organic molecules (Ferreira et al. 2019). The adsorption process between nanomaterials and different compounds is responsible for optimizing the interaction between the nanomaterial and a specific molecule (Pi et al. 2018). The literature has already shown the different compound chemical nature influences in the photocatalytic process efficiency since their protonated/deprotonated form guides the material/molecule interaction (Bian et al. 2011). Thus, anionic/cationic dyes or molecules with different lipophilicity degrees can show distinct efficiency for the same catalyst during the photocatalytic process (Wang et al. 2013, 2014). This aspect implies that the material photoactivity cannot be discussed just because of their physical-chemical properties but must be associated with the compound chemical nature to be degraded.

Materials that exhibit surfaces with a high density of negative charge can optimally disperse the reaction system, increasing the active area and, consequently, the degradation efficiency (Pi et al. 2018). However, these same materials can repel negatively-charged molecules, decrease surface interaction, and impair photocatalytic efficiency (Bian et al. 2011). Therefore, in the photocatalysis field, deepening investigations about the pollutant chemical nature and its interaction with nanomaterial can contribute to the optimization of photocatalytic processes.

In this study, Nb₂O₅ nanofibers were efficiently obtained after optimizing the electrospinning method proposed in the literature (Leindecker et al. 2014). The nanofiber photocatalytic activities were monitored for the RhB and MB dyes and the Prozac® drug (emerging pollutant) degradation, chosen for the chemical nature (MB = cationic, RhB pKa = 3.7, and Prozac® pKa = 10.7). Also, the Prozac® degradation and some of its by-products were accompanied by high-performance liquid chromatography (HPLC), which provided important information regarding the degradation mechanism mediated by Nb₂O₅ nanofibers. Details apropos the dye degradation mechanism were presented in this study, showing the importance of seeking a new statement on the Nb₂O₅ ceramic fibers application for environmental remediation. Thus, expanding studies on the material capacity to form reactive oxygen species influenced by parameters such as the reaction medium pH, the adsorption process contribution, and the degradation of different organic contaminants is a novelty.

Experimental

Nb₂O₅ ceramic nanofibers preparation

Nb₂O₅ ceramic nanofibers were fabricated by the electrospinning technique (Leindecker et al. 2014). Briefly, an alcoholic solution (10% w v⁻¹) of polyvinylpyrrolidone (PVP) was prepared using ethanol (EtOH) and methanol (MeOH). These organic solvents were selected to achieve the PVP solubility and the appropriate viscosity of the polymeric precursor. Solution viscosity was maintained between 45 to 65 cP. Then, niobium ammonium oxalate (NAO) was added to a polymeric solution in the ratio of 2:1 PVP/NAO (w:w) in 1 mL of acetic acid the viscosity of 45–65 cP. After complete solubilization, 15 mL of polymeric

blend solution (PVP/alcohol/NAO) was kept under stirring for 12 h. Then, 5 mL of blend solution was transferred into a 10 mL glass syringe with a 0.7 mm diameter metal rod needle. At a distance of 10 cm from the needle tip, a metallic cylindrical collector was covered with aluminum foil and kept under rotation for ceramic blanket formation. Here, a metal needle was connected to the electric system and submitted at a voltage of 26 kV. Simultaneously, the collector was grounded to close the electrical circuit, and the solution flow rate was maintained at 1.6 mL h^{-1} . After 40 min, the blanket form composite was collected and dried at 80°C for 12 h in the oven for solvent remotion. The blankets were calcined at 550°C for 4 h, 600°C for 3 h in a traditional muffle furnace with 2°C min^{-1} of heating/cooling rates. The obtained Nb_2O_5 ceramic fibers were named EtOH_550, EtOH_600, MeOH_550, and MeOH_600, according to solvent and the thermal-treatment temperature.

Characterization assays

The viscosity of the polymeric blend solution was measured by Brook Field viscometer. The thermal behavior of composite fibers was evaluated using TA Instruments equipment (model SDT 650). Approximately 20 mg of each sample was transferred to alumina crucible and heated from 30 to 1000°C with $10^\circ\text{C min}^{-1}$ heating rate, under 100 mL min^{-1} synthetic airflow. Structural characterization was done by X-ray diffraction (XRD), using a Shimadzu XRD 6000 diffractometer ($\text{Cu-K}\alpha / \lambda = 1,5406 \text{ \AA}$), 30 kV operating voltage, 30 mA tube current, $10\text{--}85^\circ$ angular scan (2θ interval), and $0.02^\circ \text{ min}^{-1}$ dislocation. Crystallite size was calculated using the Scherrer equation (Hargreaves 2016), and the lattice parameters obtained using Bragg's law (Stern 1978). Raman spectroscopy was applied to evaluate the nanofiber crystalline structures in the short-range order. The assays were realized a Renishaw spectrophotometer (model RM 2000) with backscattering in the region of $100\text{--}4000 \text{ cm}^{-1}$, an argon laser of $1 \mu\text{m}^2$ area, and a wavelength spot 632.8 nm as the excitation source. Nanofiber morphologies were characterized by Field Emission Gun Scanning Electron Microscopy (FEG-SEM) using a Jeol microscope (model JSM-6701F). Moreover, the presence of functional groups on the material surface was analyzed by Fourier Transform Infrared Spectroscopy (FTIR) using a Bruker Equinox 55 spectrometer. The spectra were obtained between 4000 and 400 cm^{-1} , adjusted in the transmittance module, 4 cm^{-1} resolution, and 32 scans. Zeta potential was obtained using a Zetasizer nano-ZS analyzer (Malvern Instruments, UK) with dropwise addition of 0.1 mol L^{-1} HCl or NaOH solution for pH = 1 to 10 adjustment. Nitrogen (N_2) adsorption and desorption analyzes were performed by the Brunauer Emmett and Teller (BET) method on Micromeritics equipment (ASAP 2000 model). A 160 mg of each sample was oven-dried at 80°C for 12 hours under vacuum and subsequently evacuated at a rate of $1.36 \times 10^{-3} \text{ bar s}^{-1}$ for 60 min. The samples were analyzed by applying a heating rate of $10^\circ\text{C min}^{-1}$ up until 200°C . The material optical properties were investigated by diffuse reflectance spectroscopy (DRS) in the UV-Vis region. The data were obtained on a UV-Vis spectrophotometer (Shimadzu, UV-2600) in the range of 200 to 800 nm. The Kubelca-Munk equation was used to calculate the bandgap of the material (Kumari et al. 2020). Additionally, photoluminescence (PL) measurements on the solid samples were performed using a spectrometer model QE65000 (Ocean Optics), with excitation at $\lambda = 405 \text{ nm}$ and 100 mW laser power.

The emission was collected in the 450 to 800 nm range. The PL band best adjustments were obtained by the Voigt equation area (McPhie 2000).

Photolytic and photocatalytic assays

The photolytic and photocatalytic assays under UV (254 nm, 0.94 mW cm⁻²) light were performed in a reactor described in the literature (Moreira et al. 2018), with temperature control at 18°C. Photocatalytic assays evaluated catalytic activity for MB and RhB dyes and the Prozac® (emerging pollutant).

Dyes photodegradation

3 mg L⁻¹ MB or 5 mg L⁻¹ RhB solutions were prepared by dissolving the reagent (98%, Synth) in ultrapure water. For the photocatalytic assay, 10 mg of the Nb₂O₅ nanofibers were added to a glass beaker and dispersed in 20 mL of the MB or RhB solution under constant stirring. Samples were stirred for 0.5 h (MB) or 12 h (RhB) in the dark for prior adsorption. After that, samples were irradiated in the time interval of 0.25 to 5 h (RhB) or 15 to 90 min (MB). At each time interval, an aliquot of the sample was collected and analyzed by molecular absorption. After analysis, the samples were returned to the beaker for the new irradiation interval to keep the constant volume. Molecular absorption spectra of the dyes were scanned in the 200 to 800 nm range using a Shimadzu – 1601PC spectrophotometer.

Also, a reuse study of up to 4 cycles was applied to evaluate the extended photoactivity of the catalyst that showed better performance. Therefore, the material recovered after each cycle was washed with distilled water (1 time), pure ethanol (2 times), and dried at 60°C for 12 h, before a new application of 300 min for RhB and 90 min MB.

Prozac® photodegradation

Prozac® (98 %, Santa Cecilia pharmacy), 4-Trifluoromethyl phenol (TFMP), MAEB, and 3-phenylpropyl methylamine (PPMA) solutions were separately prepared by dissolving the pure reagents (all > 97%, Sigma-Aldrich) in ultrapure water. Then, 10 mg L⁻¹ of Prozac® solution was applied in the photocatalytic assays, while TFMP, MAEB, and PPMA were used for calibration curve preparation by HPLC with UV-Vis detection (205 nm). More details on the analytical methodology and solution preparations can be obtained from the literature (Moreira et al. 2020a). For the photocatalytic assay, 5 mg of the Nb₂O₅ nanofibers were dispersed in 10 mL of Prozac® solution (10.0 mg L⁻¹) under constant stirring and kept in the dark for 30 min. Then, samples were irradiated in the time interval of 3 to 120 min, filtered in 0.22 µm membrane for catalyst removal, and subjected to chemical analysis by HPLC. Finally, dye or Prozac® solutions with pH-adjusted were obtained by dropwise addition of 0.1 mol L⁻¹ HCl or NaOH solution and monitored by a potentiometer coupled to a glass membrane electrode. Hydroxyl radical probe assay was performed following the literature method (Moreira et al. 2020b).

Results And Discussion

Structural characterization

X-ray diffraction patterns of the Nb_2O_5 ceramic fibers were indexed according to JCPDS 30–0873 (Fig. 1). The highest intensity peaks were observed at $2\theta = 22.7^\circ$, 28.5° , and 36.7° attributed to the orthorhombic phase ($\text{T-Nb}_2\text{O}_5$) (Zeng et al. 2017). The intense and well-defined lines (001), (180), and (181) showed the crystalline nature of the materials that was influenced neither by solvents (MeOH or EtOH) nor by heat treatment temperature (550 or 600°C). These results corroborated the higher thermal stability of the ceramic material above 550°C (Fig. S1). Due to a mass loss above 90% for the polymeric blanket by successive thermal events, a complete elimination of organic matter according to the infrared spectra (Fig. S2) was observed. This study revealed that the confirmation of Nb_2O_5 ceramic fiber crystalline behavior agrees with the reported literature (Nowak and Jaroniec 2008; Leindecker et al. 2014).

Figure 1.

Figure 1b shows the Raman shifts for Nb_2O_5 ceramic materials. The angular vibrations $^{\text{v}}(\text{Nb}-\text{O}-\text{Nb})$ between peaks 227 and 316 cm^{-1} were assigned to the NbO_4 tetrahedron. Peaks at 697 cm^{-1} were attributed to the $\text{||}(\text{Nb}-\text{O})$ symmetrical stretches of the $(\text{NbO}_6^{-7}; \text{NbO}_7^{-9}; \text{NbO}_8^{-11})$ polyhedra, and the peak at 803 cm^{-1} was ascribed to the symmetrical stretching of the $\text{||}(\text{Nb}=\text{O})$ surface group (Lopes et al. 2014; Hossain et al. 2019). The Raman spectra corroborate to XRD, showing the Nb_2O_5 orthorhombic phase exclusively in all samples. The unit cell parameters (a , b , and c) were calculated for EtOH_{550} , EtOH_{600} , MeOH_{550} , and MeOH_{600} . The average value of the four samples was (a) = $6.24 \text{ \AA} \pm 0.01$, (b) = $28.94 \text{ \AA} \pm 0.04$ and (c) = $3.93 \text{ \AA} \pm 0.01$, showing the similarity between them. When comparing the average values of (a), (b) and (c) with those reported in JCPDS 30–0873, the approximation was 99% (a), 101% (b) and 100% (c). Thus, the results of structural characterization confirm that the orthorhombic phase with high crystallinity was obtained for all samples, and therefore, the application in heterogeneous photocatalysis shows potential since the literature has already confirmed the $\text{T-Nb}_2\text{O}_5$ photoactivity (Lopes et al. 2014; Shao et al. 2014)

Morphological characterization

Figure 2 showed the FEG-SEM images of the EtOH_{550} , EtOH_{600} , MeOH_{550} , and MeOH_{600} samples, confirming the Nb_2O_5 nanometric fibers ($< 90 \text{ nm}$) obtaining. In the current study, the fiber diameter was reduced by 40% compared to the similar synthesis method used to produce Nb_2O_5 (Leindecker et al. 2014). This characteristic is preferred in photocatalysis studies since materials with a smaller diameter show a superior surface area.

Figure 2.

According to Table 1, the average sample diameters treated at 550°C were 35% smaller than the treated at 600°C . However, the samples processed in EtOH (550 and 600°C) showed a fiber diameter of 15% smaller, concerning the samples processed in MeOH under the same temperature conditions. These results indicated that the methanol ($\text{MeOH} = 64^\circ\text{C}$), the lowest boiling point solvent, is volatilized more efficiently than ethanol ($\text{EtOH} = 78^\circ\text{C}$), favoring the Nb_2O_5 crystal agglomeration. However, this same heat treatment

temperature did not significantly influence the crystallites size (Table 1). Thus, the fiber diameter increased due to the particle agglomeration degree obtained after the polymeric structure decomposition.

Table 1
Crystallite diameter calculated according to the Scherrer method, fiber diameter obtained by measuring n counts ($n = 100$) of the FEG-SEM images and BET surface area.

Sample	crystallite diameter* (nm)			fiber diameter (nm)	area BET ($\text{m}^2 \text{ g}^{-1}$)
	(001)	(180)	(181)		
EtOH_550	18.78	13.96	15.22	47.0 ± 0.7	37.4 ± 0.4
EtOH_600	24.00	15.14	16.04	72.0 ± 0.5	37.8 ± 0.4
MeOH_550	19.09	13.56	14.49	56.0 ± 0.7	40.5 ± 0.6
MeOH_600	22.79	14.16	15.22	85.0 ± 1.7	32.6 ± 0.3

* Scherrer diameter

Table 1.

Samples processed with EtOH showed a surface with homogeneous roughness (inset) and without holes (Fig. 2b). Therefore, the Nb_2O_5 growth and particle organization occurred more homogeneously to form the ceramic fibers. As MeOH is the most volatile, the obtained fibers with these solvents showed superficial deformations (Fig. 2d) and small holes distributed heterogeneously along with the structure (inset). Consequently, ceramic fibers with large SSA values were obtained, increasing the material potential for heterogeneous photocatalysis.

Optical characterization

The Nb_2O_5 fibers optical property was investigated by diffuse reflectance analysis. The direct bandgap energy was calculated according to the literature (Lopes et al. 2014). For all samples, the diffuse reflectance spectrum exhibited a homogeneity that corroborates with the XRD data, which showed the presence of a single crystalline phase (T- Nb_2O_5). Consequently, the average bandgap energy was $E_g = 3.87 \pm 0.04$ eV for MeOH_550, MeOH_600, and EtOH_600 samples. The EtOH_550 showed an $E_g = 3.6$ eV slightly shifted to the lower energy. Therefore, the Nb_2O_5 fibers photoactivity investigation viewing heterogeneous photocatalysis applications requires the ultraviolet wavelength.

Figure 3.

Figure 3 shows the PL spectra with top emission centers. The area percentage of each profile was adjusted using the Voigt (area) function, as described in Sect. 2.2. All PL profiles are broadband type, showing an evident relationship between the contributions of various energy levels to the electronic transition process. In Fig. 3a, the Nb_2O_5 fibers bandgap values were higher than the maximum PL

emission of each sample (\sim 2.3 to 2.6 eV) at 477 to 545 nm, respectively. Therefore, broad PL spectra cover part of the visible electromagnetic spectrum, while band-to-band electronic transitions present a slight influence. This optical phenomenon may be related to the prohibited zone additional energy levels due to the surface, interface, and bulk defects (Paris et al. 2007; Machado et al. 2017).

The differences observed in each PL spectra were treated individually with the insertion from three to six Voigt peaks, perfectly adjusted to the spectrum, as shown in Fig. 4. In all cases, a broadband emission profile in which the maximum emission, intensity, and amplitude were significantly dependent on the heat treatment temperature and solvents used in the fiber processing. Initially, there was a trend, with respect to the heat treatment variation in relation to the PL intensity ($PL_{MeOH-550} > PL_{EtOH-550} > PL_{EtOH-600} > PL_{MeOH-600}$).

Figure 4.

The samples treated at 550°C / 4h showed higher PL intensity than those treated at 600°C / 3h, which was expected due to the higher particle ordination at a higher temperature and consequent decrease in defects. For the MeOH_550 sample (Fig. 4a), the PL spectrum showed broadband and the highest intensity, with a maximum centered at 507 nm ($E_g = 2.44$ eV) in the green color. The broadband emission of the MeOH_600 sample (Fig. 4b) showed a maximum at approximately 545 nm ($E_g = 2.27$ eV), resulting in green color. This profile was the broadest of the samples analyzed, covering the most extensive spectrum from 450 to 750 nm. This effect on the PL spectrum may be due to a maximum amount of defects (surface, interface, and bulk) induced by structural changes (Phase TT-Nb₂O₅ to T-Nb₂O₅).

The Nb₂O₅ orthorhombic phase begins to crystalize at 500°C (Nico et al. 2016). In this temperature vicinity, defects arising from atomic diffusion, plane displacements, and NbO₆ octahedral distortion are susceptible. These changes were possibly responsible for showing a greater PL for the MeOH_550 than the MeOH_600 sample, in whose temperature more significant structural ordering was expected and consequent decrease in defects (Zhou et al. 2008; Joya et al. 2017).

However, samples processed with ethanol showed PL spectra with smaller intensity, following the same trend as those processed with methanol. Although the EtOH_550 (Fig. 4c) showed a PL minor intensity profile than MeOH_550, the first one also showed a broadband spectrum with a maximum of 535 nm ($E_g = 2.31$ eV) resulting in green color. This same profile was observed for EtOH_600 (Fig. 4c). However, the PL intensity was slightly lower than observed for EtOH_550. Therefore, the PL spectra changes were evidenced by processing changes in the precursors, solvents, or temperature. Finally, Nb₂O₅ fibers were evaluated to remove organic pollutants (dye and pharmaceuticals) through heterogeneous photocatalysis under UV radiation (254 nm).

Photocatalytic activity

Photocatalytic degradation of dyes

The adsorption assays (on dark) performed for RhB (12 h) and MB (0.5 h) showed that while RhB adsorption was only 1%, MB reached 18% efficacy for the different nanofibers. According to the literature, these results were shown more significant MB adsorption than RhB when other nanomaterials were applied (Choi et al. 2015; Radoń et al. 2019). Thus, after the adsorption equilibrium, the dyes were subjected to photocatalytic assays under UV light, and the degradation curves were shown in Fig. 5.

Figure 5.

The average RhB photocatalytic degradation was $47 \pm 2\%$ for Nb_2O_5 fibers in 5h (Fig. 5a), highlighting the EtOH_550 showed the best performance (49%). Only 10% of RhB was degraded in the photocatalyst absence, confirming the tendency. The MB photocatalytic degradation was up to $78\% \pm 1$ in 90 min for EtOH_550 (Fig. 5b), while the photolysis removed only 2%. First-order kinetic constants were calculated for all processes and depicted in Table 2.

Table 2
First-order kinetic constants for RhB and MB.

Sample	RhB	MB
	$k \times 10^{-3} (\text{min}^{-1}) / R^2$	$k \times 10^{-3} (\text{min}^{-1}) / R^2$
Photolysis	$0.17 \pm 0.04 / 0.848$	*
EtOH_550	$1.77 \pm 0.06 / 0.996$	$12.9 \pm 0.7 / 0.987$
EtOH_600	$1.55 \pm 0.12 / 0.983$	$6.7 \pm 0.4 / 0.986$
MeOH_550	$1.61 \pm 0.08 / 0.992$	$10.5 \pm 0.8 / 0.974$
MeOH_600	$1.43 \pm 0.07 / 0.992$	$10.7 \pm 0.1 / 0.999$

* due to insignificant removal, the slope was not obtained.

Table 2.

The kinetic constants for all Nb_2O_5 fibers are shown in Table 2, confirming photocatalytic activity against RhB and MB degradation. EtOH_550 efficiency was highlighted due to the highest kinetic constants for RhB ($1.77 \times 10^{-3} \pm 0.06 \text{ min}^{-1}$) and MB ($12.9 \times 10^{-3} \pm 0.7 \text{ min}^{-1}$). The best performance for EtOH_550 corroborates with the smaller fibers diameter, large surface area, and reduced bandgap (Tables 1 and 2). When comparing the highest kinetic constants obtained for RhB and MB, an average increase of $84\% \pm 3$ was confirmed. Confirmed the best performance for EtOH_550 against the RhB and MB degradation, this material was selected for the study of reuse of up to 4 cycles. Figure 6 shows that the RhB and MB removal after the 4 cycles were $45 \pm 3\%$ and $74 \pm 2\%$, respectively. Simultaneously, the slight variation observed in the removal (%) after each cycle can be attributed to the minor material loss after the successive transfers. Therefore, these results indicate the maintenance of the EtOH_550 catalytic activity even after 1200 min for RhB and 360 min for MB.

Figure 6

Notably, the EtOH_550 performance was very different for the degradation of the different dyes in the investigated condition ($\text{pH} = 6$), suggesting that its performance was not associated with the material physicochemical properties. Thus, this enhanced catalytic performance of the fibers associated with the dye chemical nature may have been the factor responsible for influencing the process efficiency. As the RhB charge can be changed by the $-\text{COOH}$ group protonation/deprotonation, the influence of pH was investigated.

pH evaluation

RhB and MB are cationic dyes that negative nanoparticle surfaces can attract to optimize the photocatalytic processes. However, only RhB presents a carboxylic acid group that can be deprotonated and increases the negative charge density in this molecule at $\text{pH} > \text{pKa} = 3.7$ (Obregón and Colón 2013; Aguilar et al. 2014). Then, the RhB (5 mg L^{-1}) and MB (3 mg L^{-1}) solutions were evaluated respectively for 5 h and 1.5 h to investigate the photocatalytic response at different pH conditions ($\text{pH} = 3, 6, \text{ or } 9$), using EtOH_550 sample (Fig. 6).

Figure 7.

According to Fig. 7, the photocatalytic process was efficient for RhB and MB degradation in all pH conditions. When $\text{pH} \sim \text{pKa} = 3.7$, RhB molecules transit in their protonated or neutral form, facilitating the interaction with oxidizing species responsible for the dye degradation (Obregón and Colón 2013). In alkaline conditions, the $-\text{COOH}$ group deprotonation increases the dye lipophilicity and significantly decreases the degradation rate (Aguilar et al. 2014). However, catalyst presence showed the best response for RhB degradation results under very different pH conditions (Fig. 7a). The RhB removal was 87% for $\text{pH} = 3$ and 72% for $\text{pH} = 9$, while the photocatalytic process performance was increased up to 28% and 59% compared to photolytic, respectively. This performance observed for the RhB photocatalytic degradation at alkaline pH was similar for MB degradation under the same conditions (Fig. 7b). MB photolytic degradation was insignificant at 6 and 9 pH. Simultaneously, the addition of the EtOH_550 catalyst showed to improve performance up to 76% for $\text{pH} = 6$ and 93% for $\text{pH} = 9$ compared to the photolytic process. Therefore, Nb_2O_5 fibers were essential to MB efficient degradation, confirming the effectiveness as a catalyst for the dye degradation process.

In contrast to the RhB, the MB does not show the $-\text{COOH}$ group affected by the acid-base equilibrium reaction, presenting a strictly cationic molecular structure. This aspect draws attention to the dissimilar performances, suggesting that the different dye charge distribution was the parameter responsible for optimizing the degradation process in an alkaline pH. Therefore, to better understand the pH influence in the photocatalytic process, the zeta potential of the EtOH_550 fibers was measured in the $\text{pH} = 1$ to 10 range (Fig. 7c). The zero charge point was identified at $\text{pH} \sim 2$, while the negative surface was confirmed in all conditions of $\text{pH} > 2$.

At pH = 3, RhB this protonated ($pK_a = 3.7$), optimizing the interaction with the EtOH_550 fiber which showed a slightly negative charge ($\zeta = -15 \pm 1$ mV). At pH = 9, the EtOH_550 fiber showed a significantly negative charge ($\zeta = -50 \pm 5$ mV) capable of repelling the deprotonated RhB (Merka et al. 2011). Even with the less interaction between RhB and EtOH_550 at pH = 9, the photocatalysis efficiency was confirmed, showing that $\zeta = -50 \pm 5$ mV could optimize the EtOH_550 fiber dispersion and increase the active area. This justification is applied to the efficient MB degradation at pH = 9, optimized due to the better fiber dispersions in the reaction medium. The -COOH group absence in the MB allowed the photocatalytic degradation to be 93% against the 59% observed for RhB. These RhB and MB photocatalytic degradation results follow the literature, showing the organic pollutant chemical nature is an important factor in understanding the photodegradation mechanism (Merka et al. 2011; Obregón and Colón 2013; Reeta Mary et al. 2018). Also, this increase of the negative material charge (Zeta) in less acidic conditions occurred due to the probable deprotonation of Nb-O groups that were identified by Raman analyses (Fig. 1), corroborating with the literature (Silva et al. 2019).

Due to the excellent results of dye photocatalytic degradations using EtOH_550 at pH = 9, this catalyst was applied in these conditions to degrade Prozac®. This pharmaceutical product choice was due to the high $pK_a = 10.7$ (Do et al. 2017), which preferably shows its protonated form at pH = 9 and possibly a better interaction with EtOH_550, which led to a $\zeta = -50 \pm 5$ mV. However, the -CF₃ group presence in the Prozac® molecular structure shows a negative charge density that can compete with the contribute repulsion from catalyst even for the protonated system. Thus, the photocatalytic degradation of Prozac® was investigated.

Prozac® Photocatalytic degradation

A 10 mg L⁻¹ Prozac® solution (pH = 9) was subjected to adsorption with EtOH_550 in 1 to 30 min range (Fig. 8a). The results showed an adsorption $>85\% \pm 2$ in 1 min, indicating a rapid interaction between EtOH_550 and Prozac® induced by the $\zeta = -50 \pm 5$ mV of the catalyst and the -NH₃⁺ group protonated in pH = 9 (Do et al. 2017). Then, was confirmed a 32% Prozac® desorption, previously adsorbed, until 5 min, suggesting that after the initial attraction, the -CF₃ group promoted the molecule repulsions close to the EtOH_550 surface. After this desorption step, the adsorptive process was retaken, removing Prozac® 67% ± 1 in 20 min. Finally, in 30 min, the adsorption was 68 $\pm 1\%$, showing no variation and, therefore, reaching equilibrium. Thus, before being irradiated, Prozac solutions (10 mg L⁻¹) were subjected to adsorption for 30 min.

Figure 8.

Figure 8b showed that up to 30 min, the C/Co ratio decreases considerably for both photochemical processes. Compared with photolytic, the Prozac®photocatalytic removal showed an average increase of 16% ± 1 for 3, 5, and 10 min. These results corroborate those found during the degradation of the dyes, confirming that EtOH_550 is a photoactive catalyst capable of degrading the different organic pollutants. The chromatographic analyses used to monitor Prozac® degradation also provided essential details

regarding the quantitative by-product formations. According to the literature, TFMP, MAEB, and PPMA are the main by-products formed after the Prozac® degradation (Moreira et al. 2020a) and, therefore, were quantitatively monitored in the present study.

According to the literature, the conversion from Prozac® to MAEB + TFMP preferably follows a radical oxidation mechanism, while the conversion from Prozac® to PPMA + TFMP complies with the photolytic or hydrogenation mechanism (Moreira et al. 2020a). Figure 9a shows the maximum conversion rate obtained during the Prozac® photolytic and photocatalytic degradations calculated according to the literature (Moreira et al. 2020a). The results confirm that the conversion to TFMP was more significant in both processes precisely because this is present in the two degradation mechanisms. Furthermore, the EtOH_550 catalyst presence did not influence the conversion rate to TFMP, which was similar to that found for the photolytic process. Therefore, this result suggests that the electrostatic repulsion between the -CF₃ group (present in the TFMP structure) and the EtOH_550 ($\zeta = -50 \pm 5$ mV) prevents the interaction between both, allowing the TFMP to be available in the aqueous phase for a longer time.

Figure 9.

The 1: 1 stoichiometry is expected for conversion from Prozac® to MAEB or PPMA (Moreira et al. 2020a). As different routes obtain PPMA or MAEB, the molar ratio between these by-products provides valuable information regarding the preferential Prozac® degradation mechanism. Therefore, the molar ratio [$r_{\text{molar}} = (n_{\text{MAEB}}/n_{\text{PPMA}})$] was calculated for the point of greatest conversion rate, where $r_{\text{molar}} = 0.96$ for photolytic removal and $r_{\text{molar}} = 1.5$ for EtOH_550. As the highest r_{molar} value was obtained for EtOH_550, the Prozac® oxidation mechanism mediated by hydroxyl radicals to preferentially form the MAEB was suggested. A 1.5 mg L⁻¹ coumarin solution was irradiated in the absence and presence of the EtOH_550 catalyst to support this idea, and the reaction products being monitored by photoluminescence (Fig. 8b). The PL spectra of the samples submitted to photolysis and EtOH_550 showed a peak centered at 452 nm only for EtOH_550 (Fig. 9b).

According to the literature, umbelliferone is the hydroxylation by-product of coumarin responsible at 452 nm PL emitting, and the emission is not verified in the hydroxyl radical absence (Louit et al. 2005). When adding dimethylsulfoxide (DMSO) as a radical scavenger in the reaction medium, the PL spectra (EtOH_550 + DMSO) showed the peak-centered suppression at 452 nm, confirming that the radicals were not available to umbelliferone form. Therefore, the photoactivity of EtOH_550 when exposed to UV radiation was sufficient to promote electronic excitation and generate the e⁻(CB) and h⁺(VB) pairs. These, in turn, were responsible for forming the oxidizing species capable of optimizing the Prozac® degradation for formed TFMP, PPMA, and MAEB. Finally, the Prozac® photocatalytic degradation mechanism in the presence of EtOH_550 can be represented by Fig. 10.

Figure 10.

Conclusion

Nb_2O_5 nanofibers were efficiently obtained through the electrospinning technique, and their photocatalytic property was investigated from the degradation of three organic pollutants. XRD and Raman analysis showed that the structure was consistent with the high crystallinity orthorhombic phase ($\text{T-Nb}_2\text{O}_5$). The FEG analysis confirmed the ceramic fibers form with a diameter up to $47 \text{ nm} \pm 0.7$, and BET results indicate an area up to $85.0 \text{ m}^2 \text{ g}^{-1} \pm 1.7$. The broadband PL spectra showed that different energy levels contribute to electronic transition events in the UV-vis region. When applied to RhB or MB photocatalytic degradation, the highest efficiency was obtained for EtOH_550, which degraded $47\% \pm 2$ of RhB in 5 h and $78\% \pm 1$ MB in 1.5 h. The kinetic constant in MB degradation was 86% higher than found for RhB, indicating that the strictly cationic dye was removed with greater efficiency by the catalyst. By investigating different pH conditions during photocatalytic degradation, a removal up to 87% at $\text{pH} = 3$ for RhB (5 h) and 93% for MB at $\text{pH} = 9$ (1.5 h) was achieved, suggesting the chemical nature of the dyes was the responsible factor for guiding photocatalytic efficiency. At $\text{pH} = 9$, the fibers with surface charge could be dispersed in the reaction system with greater efficiency, reaching the optimized condition to degrade the protonated molecules. Besides, due to $\text{pKa} = 10.7$ and protonated at $\text{pH} = 9$, Prozac® was subjected to photocatalytic degradation with EtOH_550. For this compound, photocatalysis was up to 17% more efficient than photolysis. Additionally, Prozac® by-products (TFMP, MAEB, and PPMA) were monitored by HPLC, and the higher forms of MAEB in the photocatalytic process were consistent with the formation of hydroxyl radicals in this system. Therefore, Nb_2O_5 nanofibers can be efficiently obtained for application in heterogeneous photocatalysis and can be an alternative material to TiO_2 , which is still the most used semiconductor in these systems.

Declarations

Ethics approval and consent to participate

Not applicable

Consent for publication

Not applicable

Availability of data and materials

The datasets used and/or analysed during the current study are available from the corresponding author on reasonable request.

Competing interests

The authors declare that they have no competing interests

Funding

Not applicable

Authors' contributions

Dr. Edson T. de Jesus: Writing, Methodology; **Dr. Ailton J. Moreira:** Writing, Methodology; **Dr^a Mayara C. Sá:** Methodology; **Dr. Gian Paulo Giovanni Freschi:** Writing - review and editing; **Dr^a Myrian R. Joya:** Writing - review and editing; **Dr. Máximo S. Li:** review and editing; **Dr^a Elaine Cristina Paris:** Writing, Conceptualization, Supervision;

Acknowledgements

The authors acknowledge to SisNano/MCTIC, Embrapa (grant # 21.14.03.001.03.00), FAPEMIG (grant # APQ-02823-14), CAPES (grant # 88887.368533/2019-00 and Code # 001), Agronano Network, and FAPEMA (BD – 08822/17).

References

- Aguilar O, Ángeles C, Castillo CO, et al (2014) On the ultrasonic degradation of Rhodamine B in water: Kinetics and operational conditions effect. Environ Technol (United Kingdom) 35:1183–1189. <https://doi.org/10.1080/09593330.2013.864711>
- Alves MCF, Souza SC, Silva MRS, et al (2009) Thermal analysis applied in the crystallization study of SrSnO₃. J Therm Anal Calorim 97:179–183. <https://doi.org/10.1007/s10973-009-0242-x>
- Bian SW, Mudunkotuwa IA, Rupasinghe T, Grassian VH (2011) Aggregation and dissolution of 4 nm ZnO nanoparticles in aqueous environments: Influence of pH, ionic strength, size, and adsorption of humic acid. Langmuir 27:6059–6068. <https://doi.org/10.1021/la200570n>
- Choi YI, Kim Y II, Cho DW, et al (2015) Recyclable magnetic CoFe₂O₄/BiOX (X = Cl, Br and I) microflowers for photocatalytic treatment of water contaminated with methyl orange, rhodamine B, methylene blue, and a mixed dye. RSC Adv 5:79624–79634. <https://doi.org/10.1039/c5ra17616f>
- Do TTT, Dao UPN, Bui HT, Nguyen TT (2017) Effect of electrostatic interaction between fluoxetine and lipid membranes on the partitioning of fluoxetine investigated using second derivative spectrophotometry and FTIR. Chem Phys Lipids 207:10–23. <https://doi.org/10.1016/j.chemphyslip.2017.07.001>
- Falk G, Borlaf M, López-Muñoz MJ, et al (2017) Microwave-assisted synthesis of Nb₂O₅ for photocatalytic application of nanopowders and thin films. J Mater Res 32:3271–3278. <https://doi.org/10.1557/jmr.2017.93>
- Fang W, Xing M, Zhang J (2017) Modifications on reduced titanium dioxide photocatalysts: A review. J Photochem Photobiol C Photochem Rev 32:21–39. <https://doi.org/10.1016/j.jphotochemrev.2017.05.003>
- Farooqui HH, Selvaraj S, Mehta A, Heymann DL (2018) Community level antibiotic utilization in India and its comparison vis-à-vis European countries: Evidence from pharmaceutical sales data. PLoS One 13:1–12. <https://doi.org/10.1371/journal.pone.0204805>

Ferreira E de P, Bessa LP, Cardoso VL, Reis MHM (2019) Influence of sintering temperature on the morphology of ceramic hollow fibers prepared from niobium pentoxide. *Int J Appl Ceram Technol* 16:781–790. <https://doi.org/10.1111/ijac.13118>

Gorito AM, Ribeiro AR, Almeida CMR, Silva AMT (2017) A review on the application of constructed wetlands for the removal of priority substances and contaminants of emerging concern listed in recently launched EU legislation. *Environ Pollut* 227:428–443. <https://doi.org/10.1016/j.envpol.2017.04.060>

Gouvêa LFC, Moreira AJ, Freschi CD, Freschi GPG (2018) Speciation of nitrite, nitrate and p-nitrophenol by photochemical vapor generation of NO using High-Resolution Continuum Source Molecular Absorption Spectrometry. *J Food Compos Anal* 70: <https://doi.org/10.1016/j.jfca.2018.04.003>

Grenni P, Ancona V, Barra Caracciolo A (2018) Ecological effects of antibiotics on natural ecosystems: A review. *Microchem J* 136:25–39. <https://doi.org/10.1016/j.microc.2017.02.006>

Grishin AM, Velichko AA, Jalalian A (2013) Nb₂O₅ nanofiber memristor. *Appl Phys Lett* 103:5–10. <https://doi.org/10.1063/1.4817302>

Gurgel MFC, Moreira ML, Paris EC, et al (2011) BaZrO₃ photoluminescence property: An ab initio analysis of structural deformation and symmetry changes. *Int J Quantum Chem* 111:694–701. <https://doi.org/10.1002/qua.22450>

Hargreaves JSJ (2016) Some considerations related to the use of the Scherrer equation in powder X-ray diffraction as applied to heterogeneous catalysts. *Catal Struct React* 2:33–37. <https://doi.org/10.1080/2055074X.2016.1252548>

Hashemzadeh F, Rahimi R, Ghaffarinejad A (2014) Mesoporous nanostructures of Nb₂O₅ obtained by an EISA route for the treatment of malachite green dye-contaminated aqueous solution under UV and visible light irradiation. *Ceram Int* 40:9817–9829. <https://doi.org/10.1016/j.ceramint.2014.02.072>

Hossain N, Günes O, Zhang C, et al (2019) Structural and physical properties of Nb₂O₅ and Nb₂O₅ thin films prepared by magnetron sputtering. *J Mater Sci Mater Electron* 30:9822–9835. <https://doi.org/10.1007/s10854-019-01319-8>

Joya MR, Barba Ortega JJ, Raba Paez AM, et al (2017) Synthesis and characterization of nano-particles of niobium pentoxide with orthorhombic symmetry. *Metals (Basel)* 7:1–9. <https://doi.org/10.3390/met7040142>

Khan AA, Tahir M (2019) Recent advancements in engineering approach towards design of photo-reactors for selective photocatalytic CO₂ reduction to renewable fuels. *J CO₂ Util* 29:205–239. <https://doi.org/10.1016/j.jcou.2018.12.008>

Kostich MS, Batt AL, Lazorchak JM (2014) Concentrations of prioritized pharmaceuticals in effluents from 50 large wastewater treatment plants in the US and implications for risk estimation. *Environ Pollut*

184:354–359. <https://doi.org/10.1016/j.envpol.2013.09.013>

Kuenemann MA, Szymczyk M, Chen Y, et al (2017) Weaver's historic accessible collection of synthetic dyes: A cheminformatics analysis. *Chem Sci* 8:4334–4339. <https://doi.org/10.1039/c7sc00567a>

Kumari N, Gaurav K, Samdarshi SK, et al (2020) Dependence of photoactivity of niobium pentoxide (Nb₂O₅) on crystalline phase and electrokinetic potential of the hydrocolloid. *Sol Energy Mater Sol Cells* 208:. <https://doi.org/10.1016/j.solmat.2020.110408>

Lapworth DJ, Baran N, Stuart ME, Ward RS (2012) Emerging organic contaminants in groundwater: A review of sources, fate and occurrence. *Environ Pollut* 163:287–303.

<https://doi.org/10.1016/j.envpol.2011.12.034>

Lee CM, Palaniandy P, Dahlan I (2017) Pharmaceutical residues in aquatic environment and water remediation by TiO₂ heterogeneous photocatalysis: a review. *Environ Earth Sci* 76:. <https://doi.org/10.1007/s12665-017-6924-y>

Leindecker GC, Alves AK, Bergmann CP (2014) Synthesis of niobium oxide fibers by electrospinning and characterization of their morphology and optical properties. *Ceram Int* 40:16195–16200. <https://doi.org/10.1016/j.ceramint.2014.07.054>

Leite ER, Paris EC, Longo E, Varela JA (2000) Direct Amorphous-to-Cubic Perovskite Phase Transformation for Lead Titanate. *J Am Ceram Soc* 83:1539–1541. <https://doi.org/10.1111/j.1151-2916.2000.tb01427.x>

Lopes OF, Paris EC, Ribeiro C (2014) Synthesis of Nb₂O₅ nanoparticles through the oxidant peroxide method applied to organic pollutant photodegradation: A mechanistic study. *Appl Catal B Environ* 144:800–808. <https://doi.org/10.1016/j.apcatb.2013.08.031>

Louit G, Foley S, Cabillic J, et al (2005) The reaction of coumarin with the OH radical revisited: Hydroxylation product analysis determined by fluorescence and chromatography. *Radiat Phys Chem* 72:119–124. <https://doi.org/10.1016/j.radphyschem.2004.09.007>

Machado TR, Sczancoski JC, Beltrán-Mir H, et al (2017) A novel approach to obtain highly intense self-activated photoluminescence emissions in hydroxyapatite nanoparticles. *J Solid State Chem* 249:64–69. <https://doi.org/10.1016/j.jssc.2016.12.018>

Malafatti JOD, Moreira AJ, Sciena CR, et al (2020) Prozac® removal promoted by HAP:Nb₂O₅ nanoparticles system: by-products, mechanism, and cytotoxicity assessment. *J Environ Chem Eng* 104820. <https://doi.org/10.1016/j.jece.2020.104820>

McPhie P (2000) Principles of Fluorescence Spectroscopy, Second ed. Joseph R. Lakowicz. *Anal Biochem* 287:353–354. <https://doi.org/10.1006/abio.2000.4850>

Merka O, Yarovy V, Bahnemann DW, Wark M (2011) pH-Control of the Photocatalytic Degradation Mechanism of Rhodamine B over Pb₃Nb₄O₁₃. *J Phys Chem C* 115:8014–8023.
<https://doi.org/10.1021/jp108637r>

Moreira A, Borges A, de Sousa B, et al (2018) Photodegradation of Fluoxetine Applying Different Photolytic Reactors: Evaluation of the Process Efficiency and Mechanism. *J Braz Chem Soc* 30:1010–1024. <https://doi.org/10.21577/0103-5053.20180250>

Moreira AJ, Campos LO, Maldi CP, et al (2020a) Photocatalytic degradation of Prozac® mediated by TiO₂ nanoparticles obtained via three synthesis methods: sonochemical, microwave hydrothermal, and polymeric precursor. *Environ Sci Pollut Res*. <https://doi.org/10.1007/s11356-020-08798-x>

Moreira AJ, Malafatti JOD, Giraldi TR, et al (2020b) Prozac® photodegradation mediated by Mn-doped TiO₂ nanoparticles: Evaluation of by-products and mechanisms proposal. *J Environ Chem Eng* 8:. <https://doi.org/10.1016/j.jece.2020.104543>

Nb O, Araújo MA De, Gromboni MF, et al (2018) Applied Catalysis B: Environmental Contrasting transient photocurrent characteristics for thin films of vacuum-. 237:339–352

Nico C, Monteiro T, Graça MPF (2016) Niobium oxides and niobates physical properties: Review and prospects. *Prog Mater Sci* 80:1–37. <https://doi.org/10.1016/j.pmatsci.2016.02.001>

Nogueira AE, Lopes OF, Neto ABS, Ribeiro C (2017) Enhanced Cr(VI) photoreduction in aqueous solution using Nb₂O₅/CuO heterostructures under UV and visible irradiation. *Chem Eng J* 312:220–227.
<https://doi.org/10.1016/j.cej.2016.11.135>

Nowak I, Jaroniec M (2008) “Hard” vs. “soft” templating synthesis of mesoporous Nb₂O₅ catalysts for oxidation reactions. *Top Catal* 49:193–203. <https://doi.org/10.1007/s11244-008-9084-1>

Obregón S, Colón G (2013) On the different photocatalytic performance of BiVO₄ catalysts for Methylene Blue and Rhodamine B degradation. *J Mol Catal A Chem* 376:40–47.
<https://doi.org/10.1016/j.molcata.2013.04.012>

Oliveira LH, Paris EC, Avansi W, et al (2013) Correlation between photoluminescence and structural defects in Ca_{1+x}Cu_{3-X}Ti₄O₁₂ systems. *J Am Ceram Soc* 96:209–217.
<https://doi.org/10.1111/jace.12020>

Paris EC, Espinosa JWM, de Lazaro S, et al (2007) Er³⁺ as marker for order-disorder determination in the PbTiO₃ system. *Chem Phys* 335:7–14. <https://doi.org/10.1016/j.chemphys.2007.03.019>

Paris EC, Gurgel MFC, Joya MR, et al (2010) Structural deformation monitored by vibrational properties and orbital modeling in (Pb,Sm)TiO₃ systems. *J Phys Chem Solids* 71:12–17.
<https://doi.org/10.1016/j.jpcs.2009.09.012>

Paris EC, Malafatti JOD, Sciena CR, et al (2020) Nb₂O₅ nanoparticles decorated with magnetic ferrites for wastewater photocatalytic remediation. Environ Sci Pollut Res. <https://doi.org/10.1007/s11356-020-11262-5>

Petrie B, Barden R, Kasprzyk-Hordern B (2015) A review on emerging contaminants in wastewaters and the environment: Current knowledge, understudied areas and recommendations for future monitoring. Water Res 72:3–27. <https://doi.org/10.1016/j.watres.2014.08.053>

Pi Y, Li X, Xia Q, et al (2018) Adsorptive and photocatalytic removal of Persistent Organic Pollutants (POPs) in water by metal-organic frameworks (MOFs). Chem Eng J 337:351–371. <https://doi.org/10.1016/j.cej.2017.12.092>

Pinheiro BS, Gimenes LLS, Moreira AJ, et al (2016) Arsenic speciation in environmental samples using different acid concentrations and ultrasonic extraction for the determination by HG-FAAS. At Spectrosc 37:

Qi S, Zuo R, Liu Y, Wang Y (2013) Synthesis and photocatalytic activity of electrospun niobium oxide nanofibers. Mater Res Bull 48:1213–1217. <https://doi.org/10.1016/j.materresbull.2012.11.074>

Raba AM, Barba-Ortega J, Joya MR (2015) The effect of the preparation method of Nb₂O₅ oxide influences the performance of the photocatalytic activity. Appl Phys A Mater Sci Process 119:923–928. <https://doi.org/10.1007/s00339-015-9041-3>

Radoń A, Łoński S, Warski T, et al (2019) Catalytic activity of non-spherical shaped magnetite nanoparticles in degradation of Sudan I, Rhodamine B and Methylene Blue dyes. Appl Surf Sci 487:1018–1025. <https://doi.org/10.1016/j.apsusc.2019.05.091>

Rauf MA, Ashraf SS (2009) Fundamental principles and application of heterogeneous photocatalytic degradation of dyes in solution. Chem Eng J 151:10–18. <https://doi.org/10.1016/j.cej.2009.02.026>

Reeta Mary I, Sonia S, Navadeepthy D, et al (2018) Surfactant-free solvothermal synthesis of Hydroxyapatite nested bundles for the effective photodegradation of cationic dyes. J Phys Chem Solids 116:180–186. <https://doi.org/10.1016/j.jpcs.2018.01.035>

Sanaullah M, Usman M, Wakeel A, et al (2020) Terrestrial ecosystem functioning affected by agricultural management systems: A review. Soil Tillage Res 196:.. <https://doi.org/10.1016/j.still.2019.104464>

Shao R, Cao Z, Xiao Y, et al (2014) Enhancing photocatalytic activity by tuning the ratio of hexagonal and orthorhombic phase Nb₂O₅ hollow fibers. RSC Adv 4:26447–26451. <https://doi.org/10.1039/c4ra02038c>

Shen R, Jiang C, Xiang Q, et al (2019) Surface and interface engineering of hierarchical photocatalysts. Appl Surf Sci 471:43–87. <https://doi.org/10.1016/j.apsusc.2018.11.205>

Silva GTST, Nogueira AE, Oliveira JA, et al (2019) Acidic surface niobium pentoxide is catalytic active for CO₂ photoreduction. *Appl Catal B Environ* 242:349–357. <https://doi.org/10.1016/j.apcatb.2018.10.017>

Stern EA (1978) Structure determination by X-ray absorption. *Contemp Phys* 19:289–310. <https://doi.org/10.1080/00107517808210887>

Védrine JC (2019) Importance, features and uses of metal oxide catalysts in heterogeneous catalysis. *Chinese J Catal* 40:1627–1636. [https://doi.org/10.1016/S1872-2067\(18\)63162-6](https://doi.org/10.1016/S1872-2067(18)63162-6)

Wang C, Zhang Y, Yu L, et al (2013) Oxidative degradation of azo dyes using tourmaline. *J Hazard Mater* 260:851–859. <https://doi.org/10.1016/j.jhazmat.2013.06.054>

Wang K, Xu J, Hua X, et al (2014) Highly efficient photodegradation of RhB-MO mixture dye wastewater by Ag₃PO₄ dodecahedrons under acidic condition. *J Mol Catal A Chem* 393:302–308. <https://doi.org/10.1016/j.molcata.2014.06.026>

Zeng GY, Wang H, Guo J, et al (2017) Fabrication of Nb₂O₅/C nanocomposites as a high performance anode for lithium ion battery. *Chinese Chem Lett* 28:755–758. <https://doi.org/10.1016/j.cclet.2017.01.001>

Zhao J, Xu H, Tang D, et al (2016) A comparative evaluation of coal specific surface area by CO₂ and N₂ adsorption and its influence on CH₄ adsorption capacity at different pore sizes. *Fuel* 183:420–431. <https://doi.org/10.1016/j.fuel.2016.06.076>

Zhou X, Li Z, Wang Y, et al (2008) Photoluminescence of amorphous niobium oxide films synthesized by solid-state reaction. *Thin Solid Films* 516:4213–4216. <https://doi.org/10.1016/j.tsf.2007.12.112>

Zhuang XJ, Xia QN, Wang YQ, et al (2016) Hydrodeoxygenation of butyric acid at multi-functional Nb₂O₅ catalyst: A density functional theory study. *Int J Hydrogen Energy* 41:18502–18508. <https://doi.org/10.1016/j.ijhydene.2016.08.220>

Figures

Fig. 1

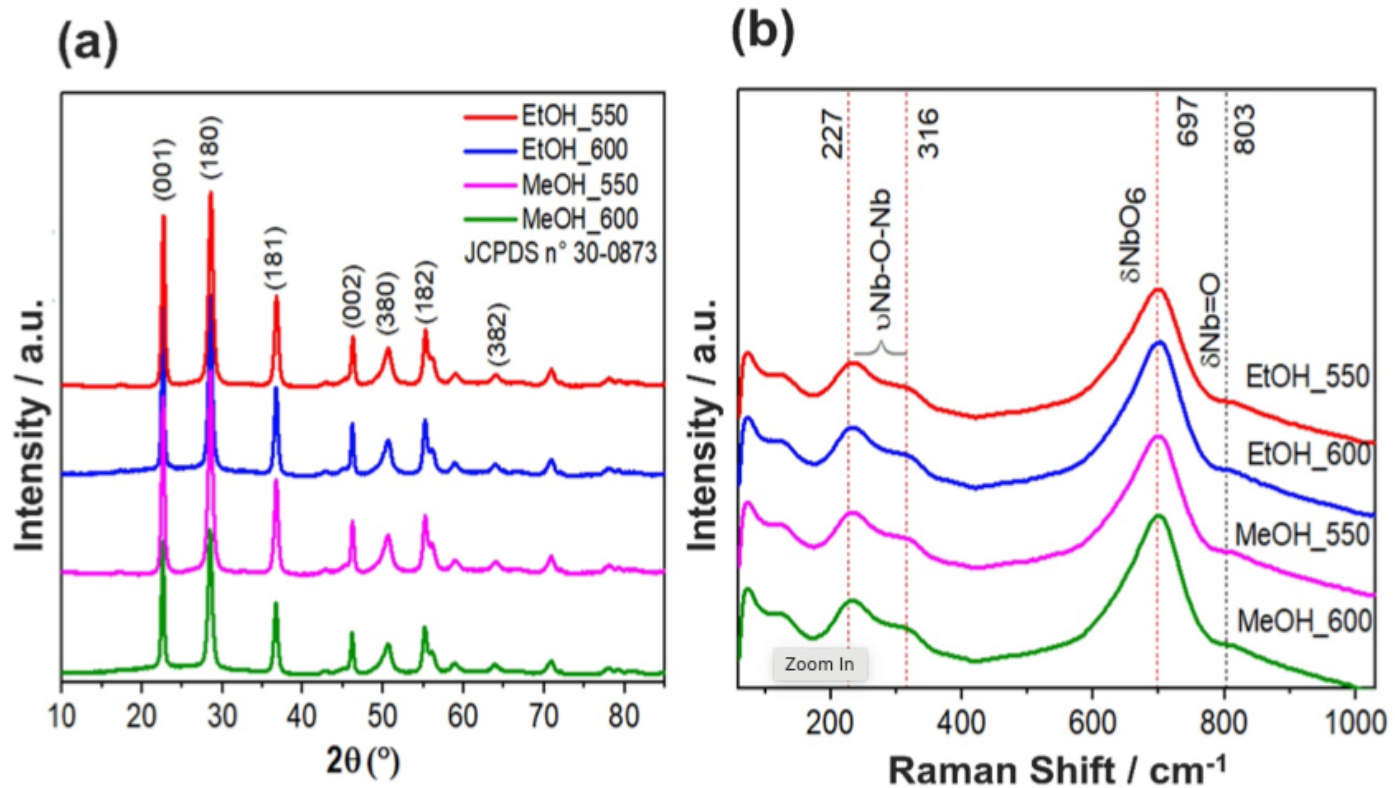


Figure 1

XRD patterns(a) and Raman spectrum (b) of the Nb₂O₅ nanofibers.

Fig. 2

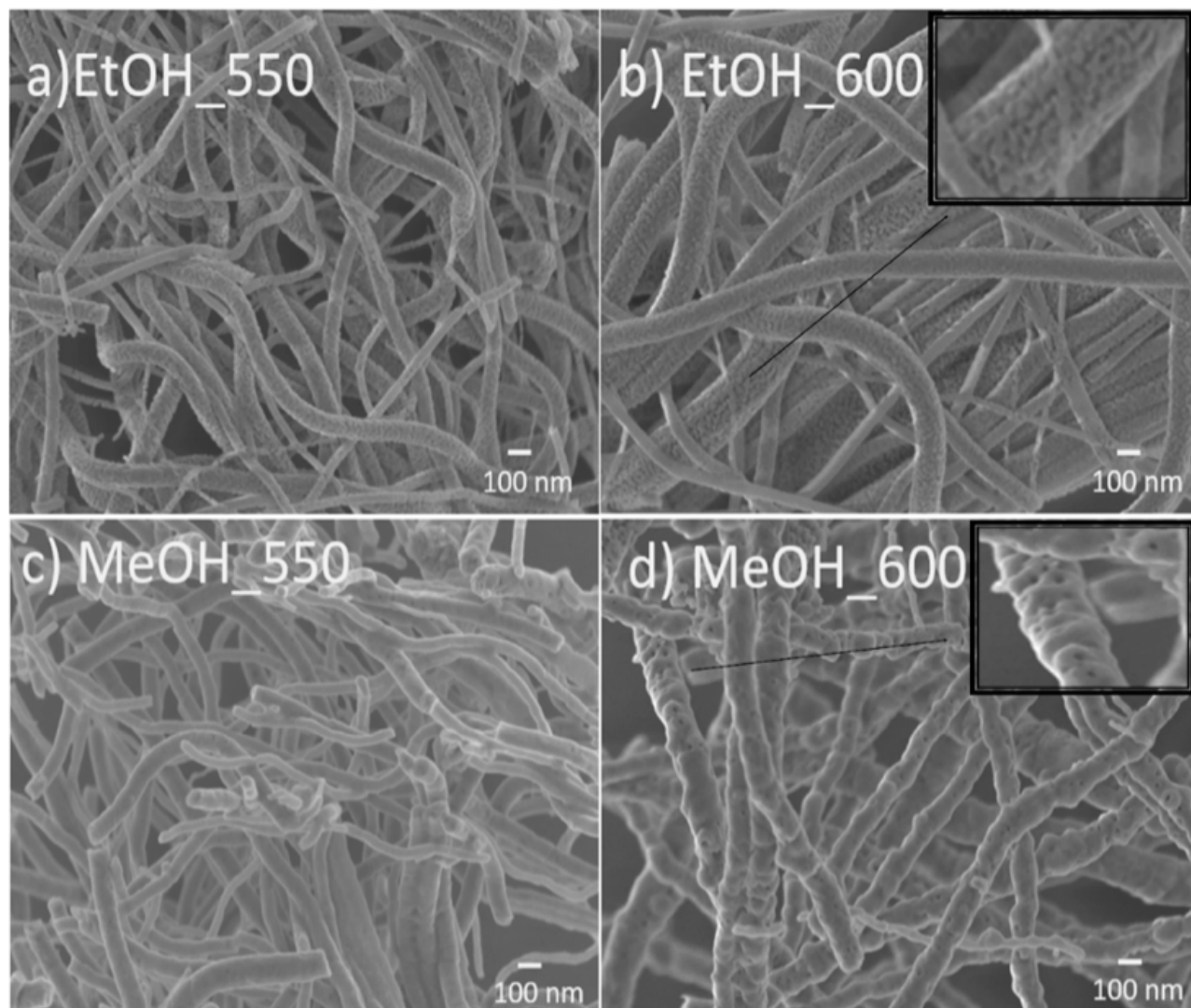


Figure 2

FEG-SEM images of the Nb₂O₅ nanofibers obtained at different solvents and calcined at 550 °C for 4 h or 600 °C for 3h.

Fig. 3

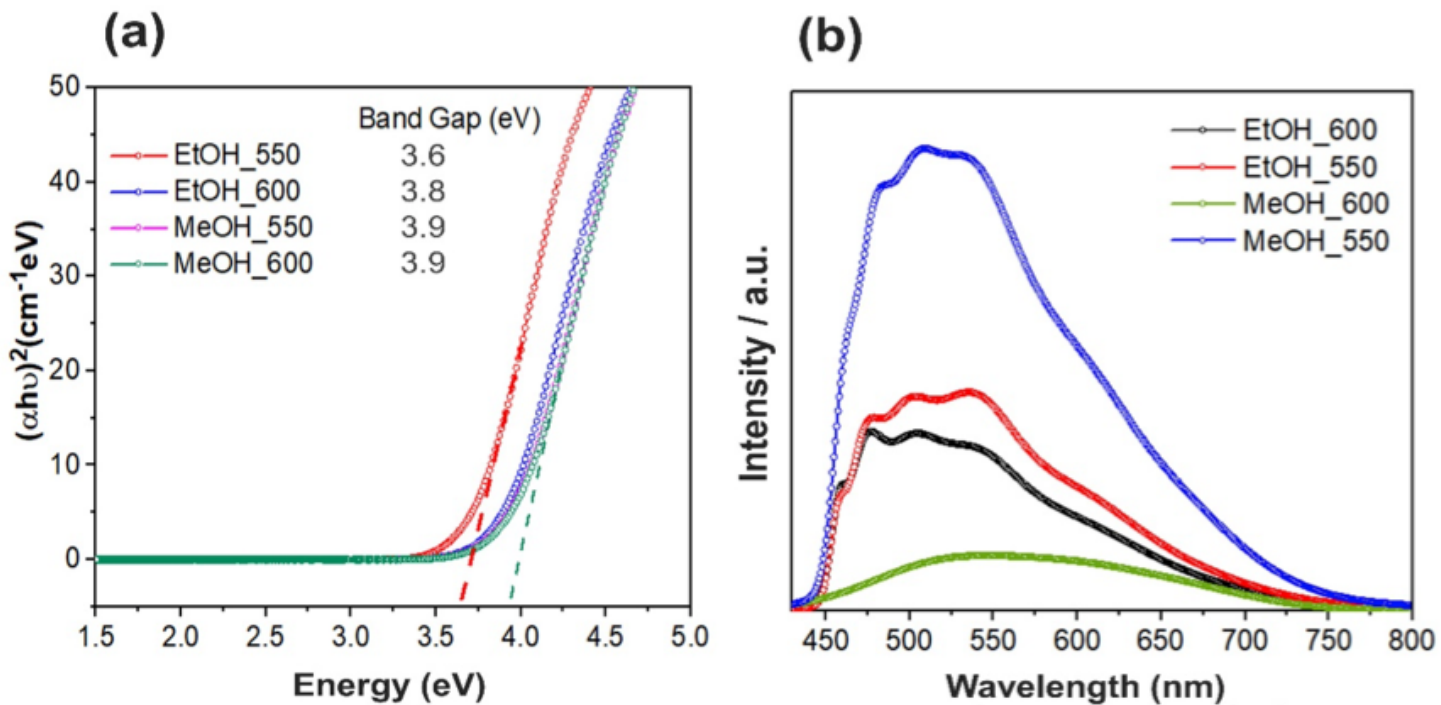


Figure 3

Variation of $(\alpha h\nu)^2$ versus $h\nu$ for direct bandgap transitions (a) and PL spectra (b) of the Nb₂O₅ nanofibers.

Fig. 4

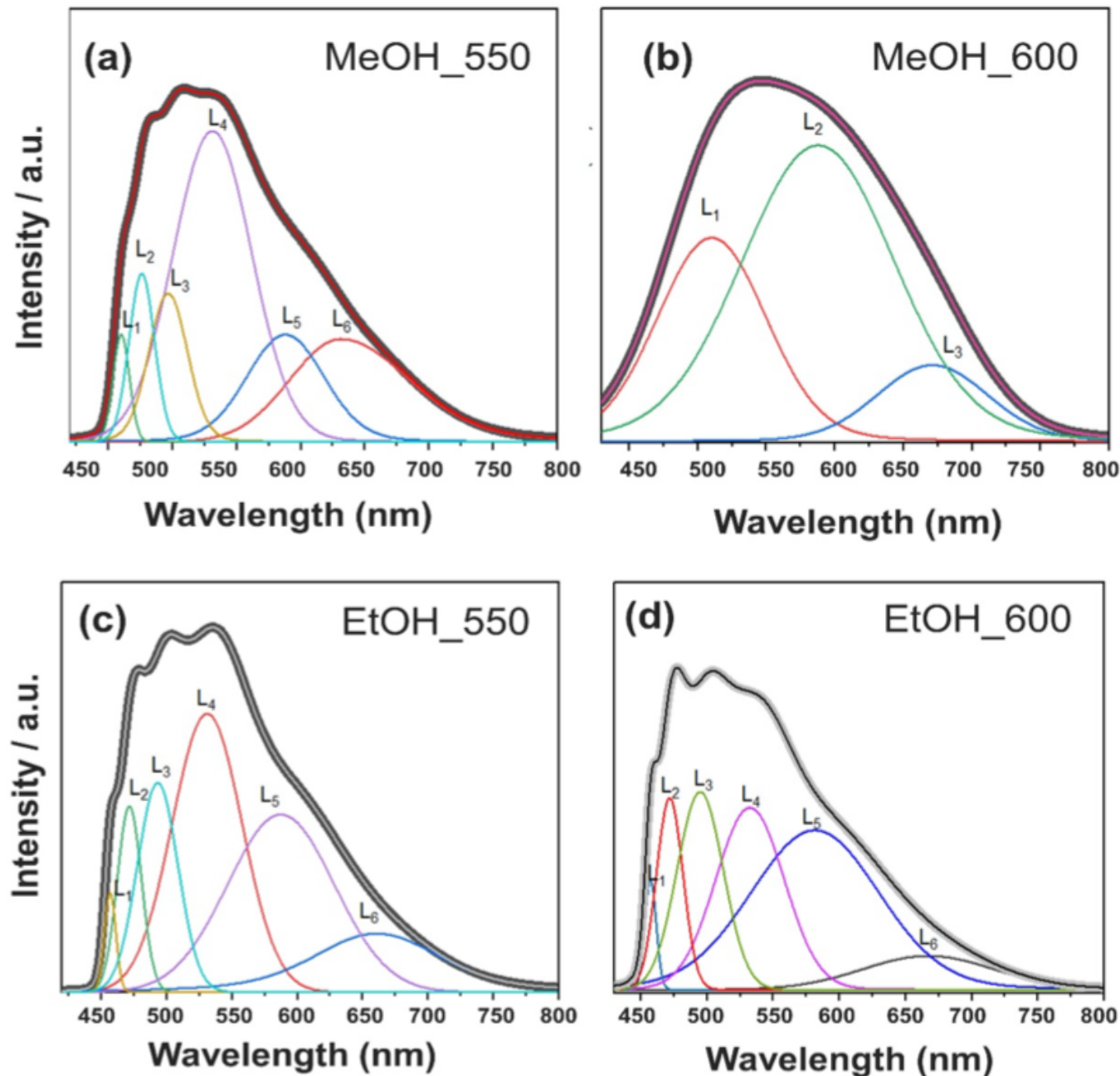


Figure 4

PL spectra for samples MeOH_550 (a), MeOH_600 (b), EtOH_550 (c) and EtOH_600 (d).

Fig. 5

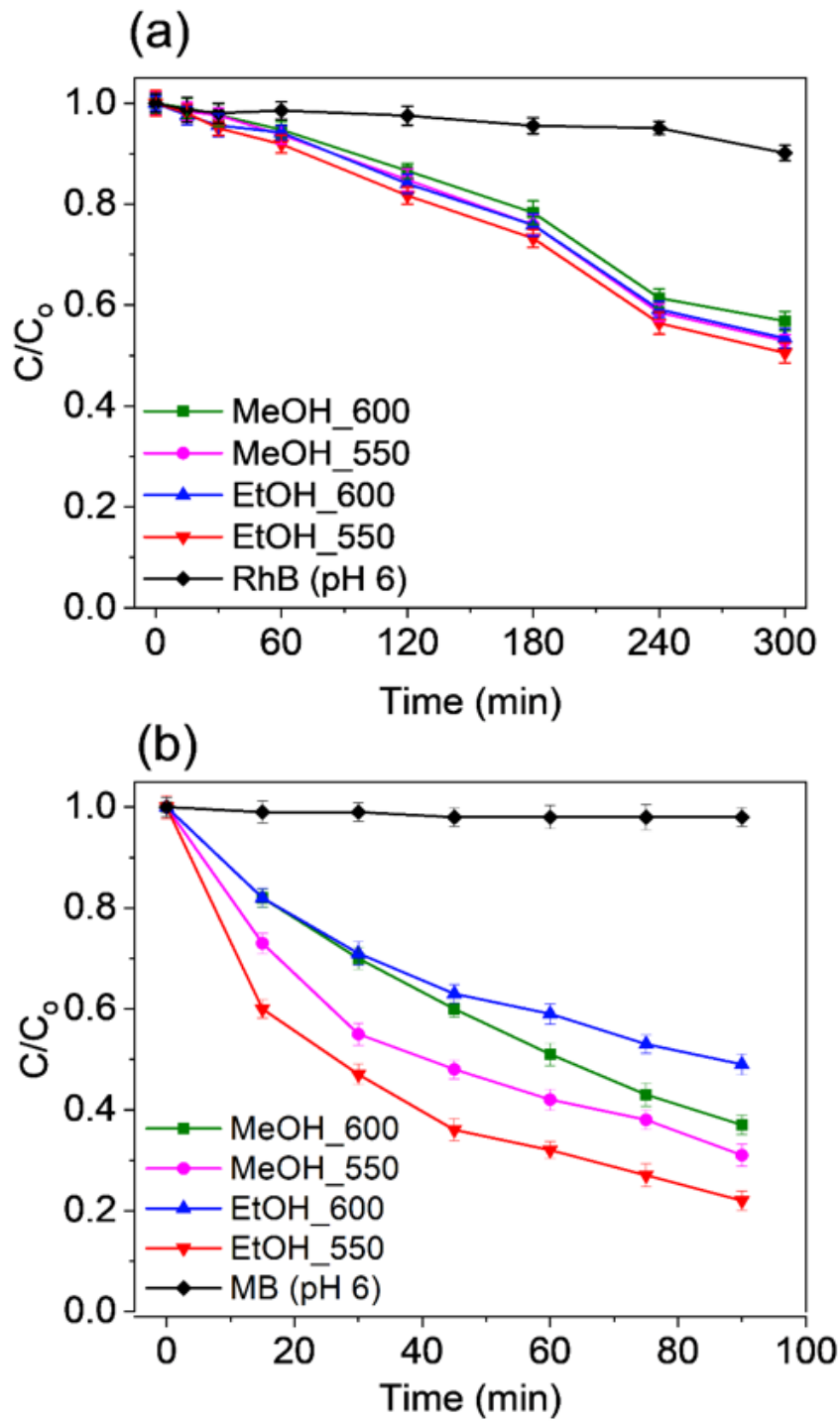


Figure 5

Decay curves of the RhB (a) and MB (b) after photolytic or photocatalytic degradation.

Fig. 6

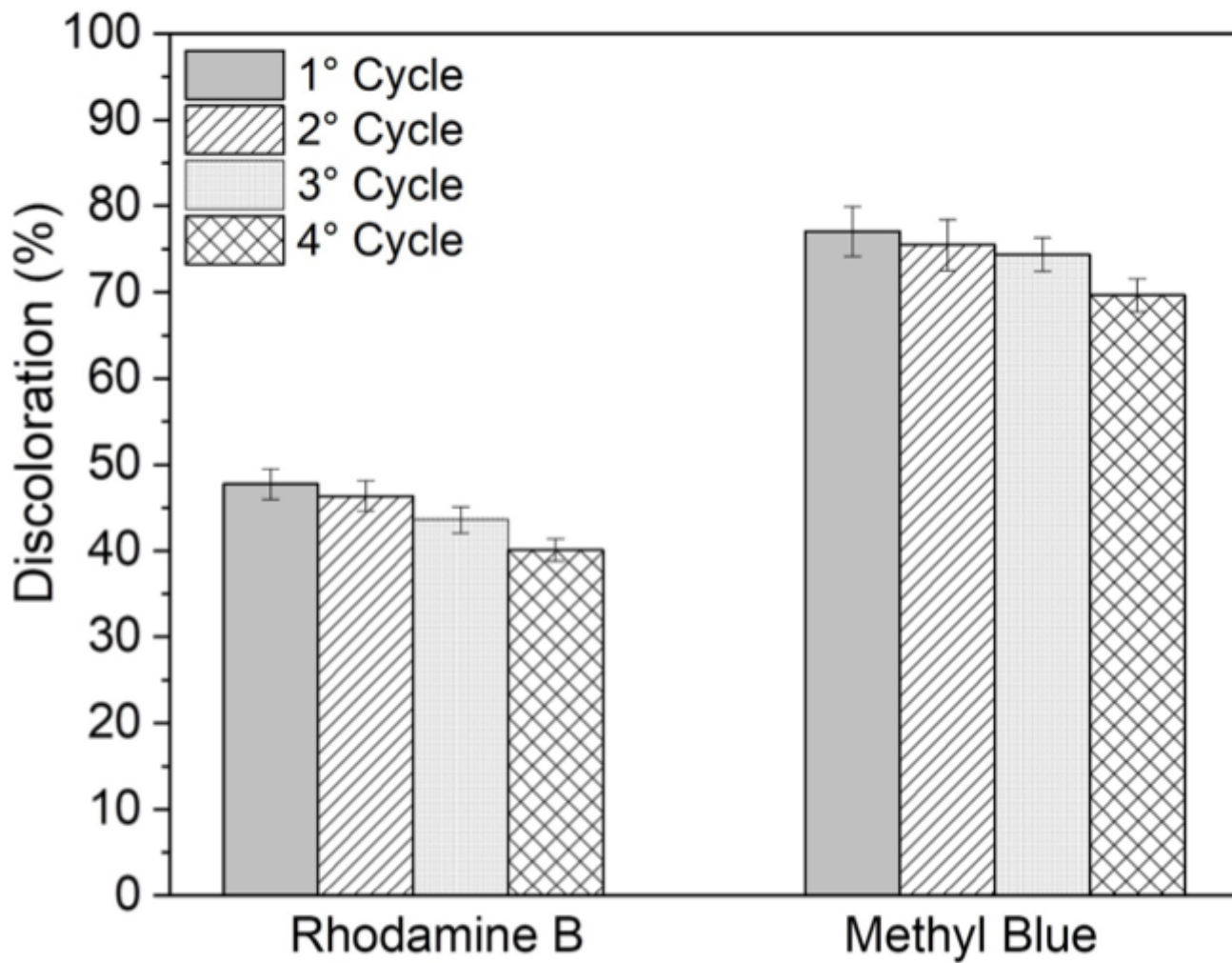


Figure 6

RhB and MB photocatalytic removal in 4 application cycles with EtOH_550 recovered. Conditions: [pH = 6, degradation time: 300 min (RhB), 90 min (MB)]

Fig. 7

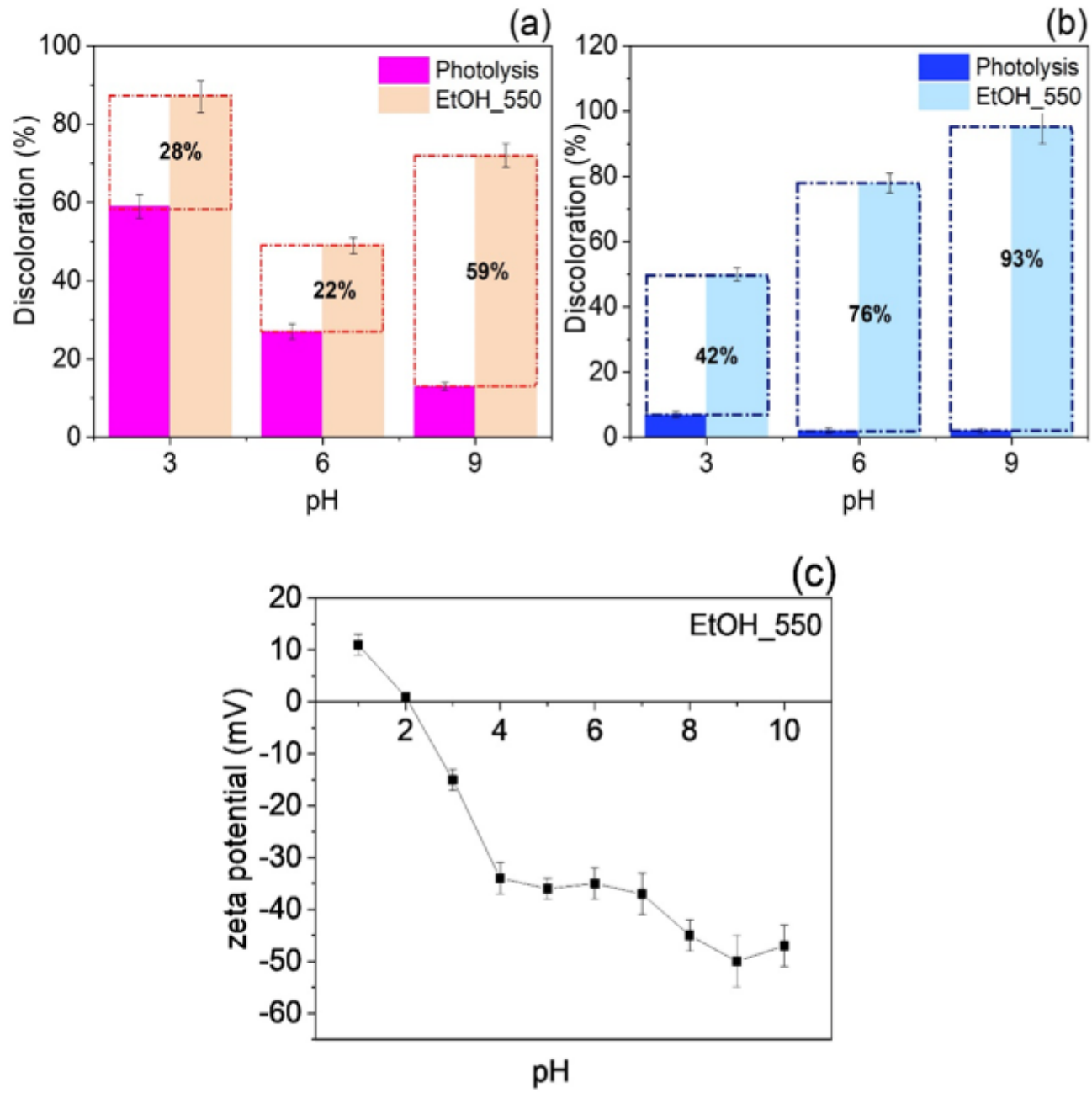


Figure 7

Photocatalytic discoloration of RhB for 5h (a) and MB for 1.5h (b) at pH = 3, 6 or 9. Zeta potential values measured at pH = 1 to 10 (c).

Fig. 8

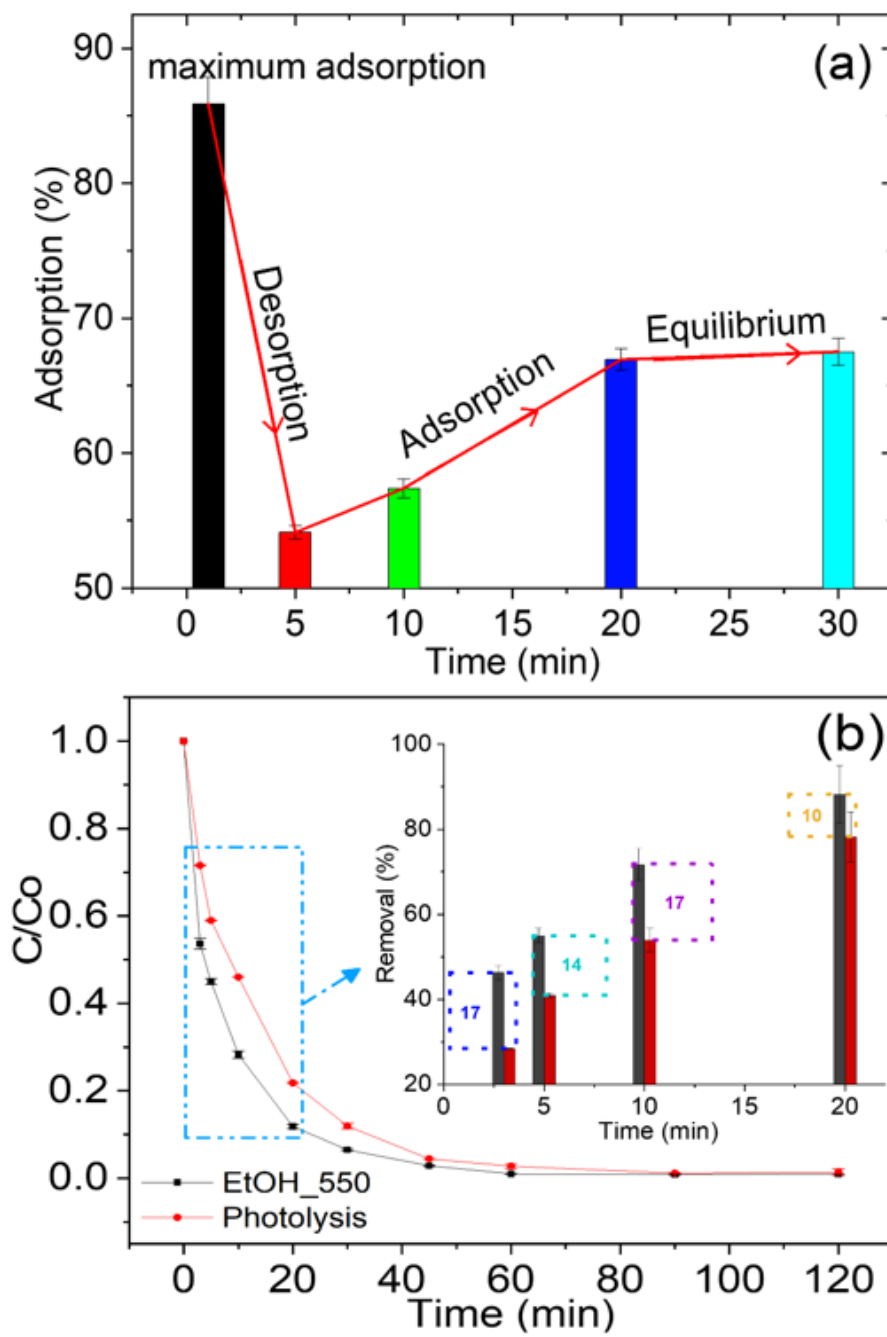


Figure 8

Adsorption of Prozac® in the time interval from 1 to 30 min (a) and decay curve during the photocatalytic process (b).

Fig. 9

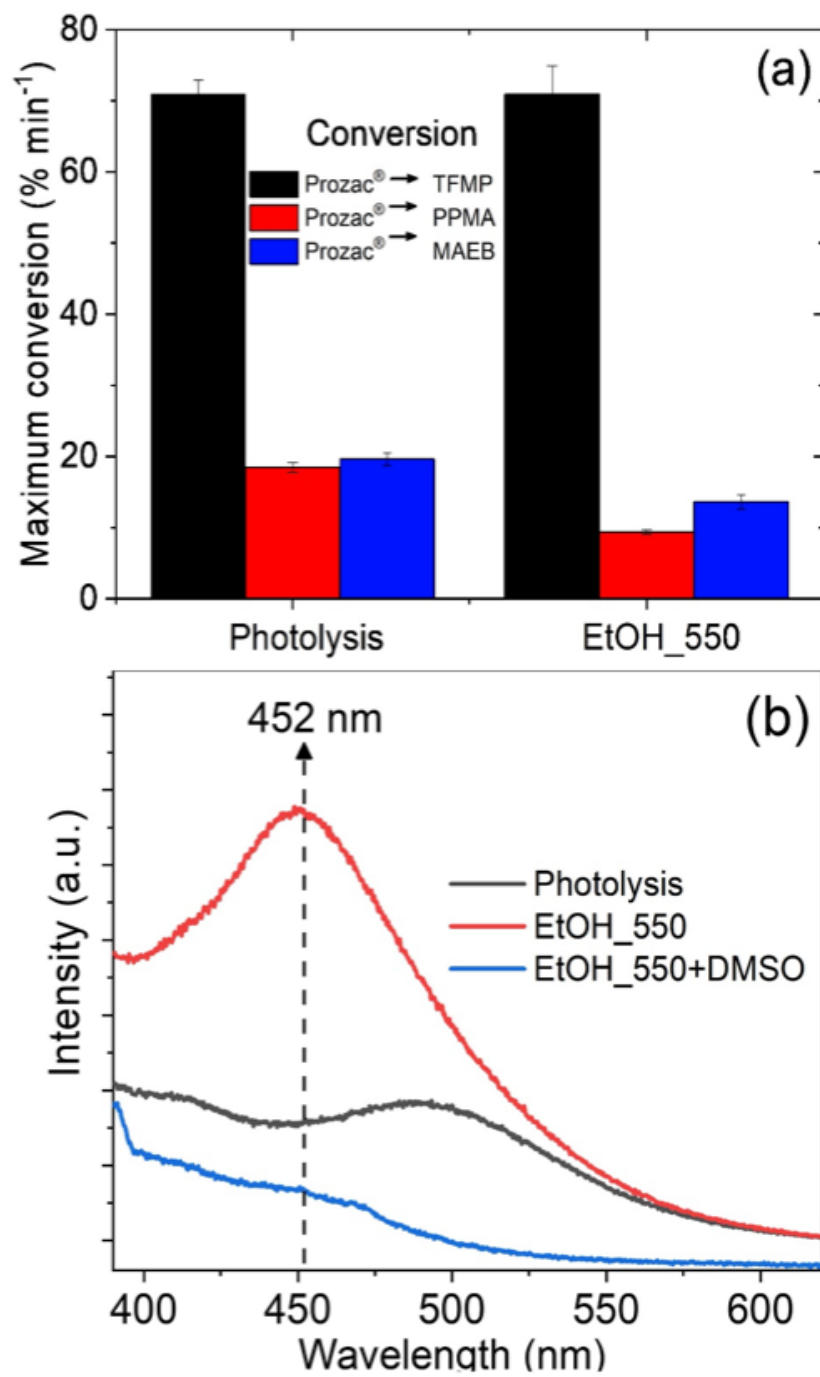


Figure 9

Maximum conversion of Prozac® to by-products (a) and PL spectrum of the umbelliferrone formed in the •OH probe assay (b).

Fig. 10.

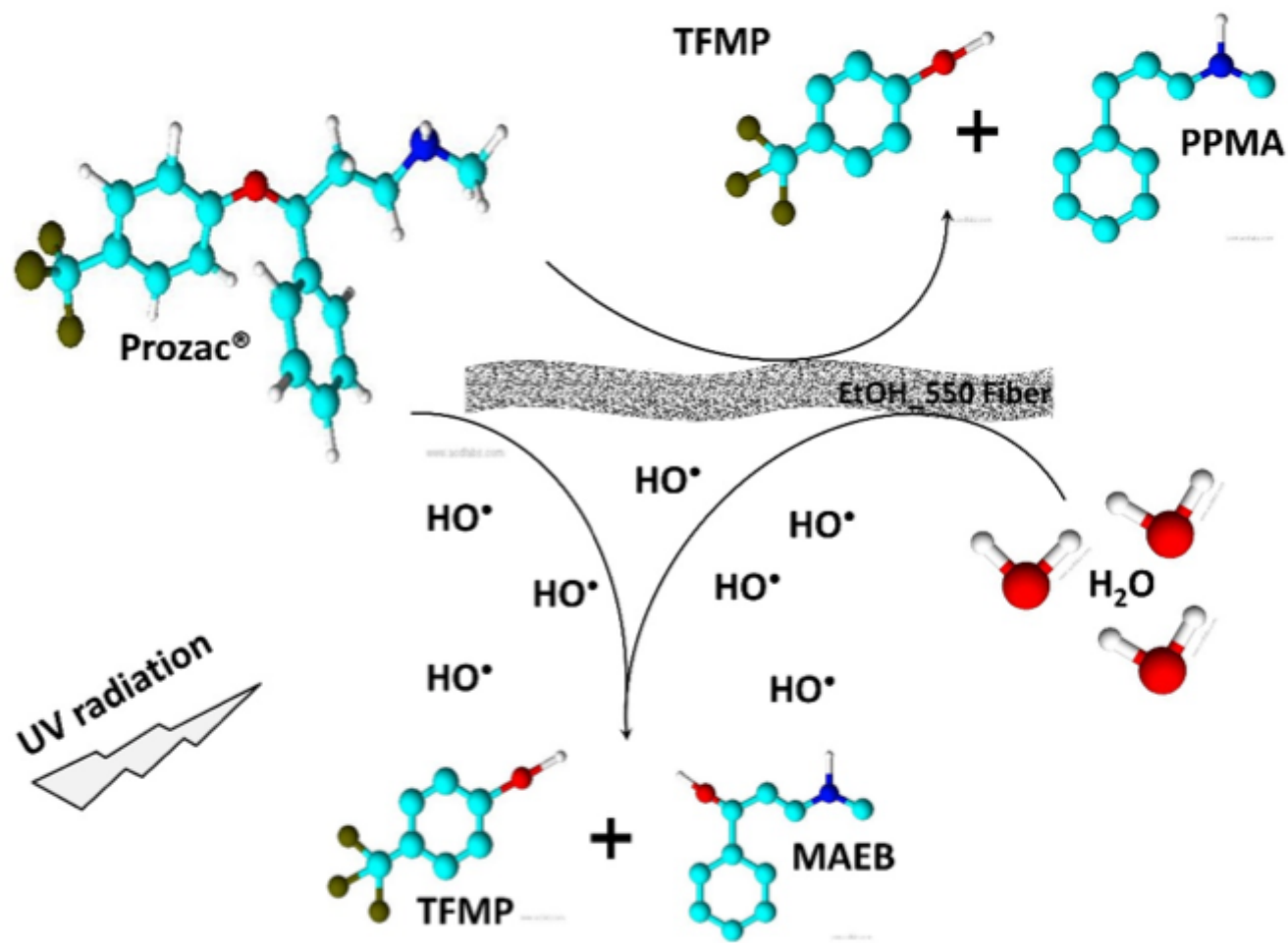


Figure 10

Degradation mechanism of Prozac® mediated by EtOH_550 fiber under UV radiation.

Supplementary Files

This is a list of supplementary files associated with this preprint. Click to download.

- GraphicAbstract.jpg
- Supplementarymaterial.docx